Effects of Differing Underlying Assumptions in In Silico Models on Predictions of DNA Damage and Repair

Document Version
Accepted author manuscript

Link to publication record in Manchester Research Explorer

Citing this paper
Please note that where the full-text provided on Manchester Research Explorer is the Author Accepted Manuscript or Proof version this may differ from the final Published version. If citing, it is advised that you check and use the publisher's definitive version.

OPEN ACCESS

Effects of Differing Underlying Assumptions in In Silico Models on Predictions of DNA Damage and Repair

AQ: au

John W. Warmenhoven,[a,b,1,2] Nicholas T. Henthorn,[a,b,1] Aimee L. McNamara,[c] Samuel P. Ingram,[a,d]
Michael J. Merchant,[a,b] Karen J. Kirkby,[a,b] Jan Schuemann,[c] Harald Paganetti,[c] Kevin M. Prise,[e]
Stephen J. McMahon[e]

[a] Division of Cancer Sciences, University of Manchester, Manchester, United Kingdom; [b] The Christie NHS Foundation Trust, Manchester Academic Health Science Centre, Manchester, United Kingdom; [c] Physics Division, Department of Radiation Oncology, Massachusetts General Hospital and Harvard Medical School, Massachusetts; [d] Christie Medical Physics and Engineering, The Christie NHS Foundation Trust, Manchester, United Kingdom; [e] Patrick G Johnston Centre for Cancer Research, Queen's University Belfast, Belfast, United Kingdom

Warmenhoven JW, Henthorn NT, McNamara AL, Ingram SP, Merchant MJ, Kirkby KJ, Schuemann J, Paganetti H, Prise KM, McMahon SJ. Effects of Differing Underlying Assumptions in In Silico Models on Predictions of DNA Damage and Repair. Radiat Res. 200, 000–000 (2023).

The induction and repair of DNA double-strand breaks (DSBs) are critical factors in the treatment of cancer by radiotherapy. To investigate the relationship between incident radiation and cell death through DSB induction many in silico models have been developed. These models produce and use custom formats of data, specific to the investigative aims of the researchers, and often focus on particular pairings of damage and repair models. In this work we use a standard format for reporting DNA damage to evaluate combinations of different, independently developed, models. We demonstrate the capacity of such inter-comparison to determine the sensitivity of models to both known and implicit assumptions. Specifically, we report on the impact of differences in assumptions regarding patterns of DNA damage induction on predicted initial DSB yield, and the subsequent effects this has on derived DNA repair models. The observed differences highlight the importance of considering initial DNA damage on the scale of nanometres rather than micrometres. We show that the differences in DNA damage models result in subsequent repair models assuming significantly different rates of random DSB end diffusion to compensate. This in turn leads to disagreement on the mechanisms responsible for different biological endpoints, particularly when different damage and repair models are combined, demonstrating the importance of inter-model comparisons to explore underlying model assumptions.   © 2023 by Radiation Research Society

INTRODUCTION

DNA strand breaks pose a significant threat to a cell's survival and as such many complex mechanisms have evolved to restore the double-helix structure (*1*, *2*). Double-strand breaks (DSBs) are the most challenging damages to repair, which if handled inappropriately can lead to chromosomal aberrations and persistent, or residual, breaks. Both chromosomal aberrations and residual DSBs contribute to cell death (*3–6*). Thus, it is the induction of DSBs by ionising radiation which is exploited in radiotherapy to deliver a lethal dose to a tumour volume. The number of DSBs induced by radiation has long been thought to be the dominant influence on cell death (*7*).

In the context of hadron therapy, the relative biological effectiveness (RBE) of different radiations is of critical importance to determine the doses prescribed clinically. RBE is simply the ratio of doses required to produce the same biological effect, usually referenced against conventional X-ray therapy. This ratio is known to vary with parameters such as the linear energy transfer (LET) of radiation (*8*). The biological mechanisms that lead to this observed difference in RBE are not well understood. Aspects of both the creation of DSBs and the subsequent repair have been implicated (*9*, *10*). Moreover, with an increasing variety of particles investigated, the possibility that different particles of similar LET produce different biological outcomes has been raised (*11–14*). Although caution should be taken when comparing such experimental data, both because of the variance endemic to the field [see the PIDE database (*15*)], and because others have suggested that elements of the experimental set-up could have contributed to the observed differences (*16*). These uncertainties necessitate a deeper understanding of the involved mechanisms to better exploit the different RBE of radiotherapy modalities available clinically. Past advances in understanding have led to novel targeted therapies of drugs in combination with radiation (*17*, *18*), as well as identification of genetic phenotypes predisposed to cancer (*19*, *20*).

In silico modelling of complex biological systems provides an effective method of forming and refining hypotheses to be

[1] These authors contributed equally to this article.
[2] Corresponding author: John W. Warmenhoven, The University of Manchester, Manchester, United Kingdom; email: john.warmenhoven@manchester.ac.uk.

0

0   WARMENHOVEN ET AL.

tested experimentally. The tight control of experimental conditions in such models allows investigation of the sensitivity to specific parameters in the absence of confounding factors that would otherwise serve to obscure causal relationships. Furthermore, in silico models allow us to link mechanisms operating at scales challenging to resolve in state-of-the-art in vitro or in vivo experiments to more readily observable effects that can validate underlying hypotheses.

Such models are widely used in radiotherapy research, with many institutions separately developing their own custom codes. A wide range of modelling approaches and data formats are used, relevant to each institutes' research interests. For reviews comparing such models on a high level, see work by Stewart et al. (21) and Friedland et al. (22). Models can be categorized on a scale from highly abstract to least abstract, with clinical acceptance generally following inversely with the level of abstraction.

Starting with the most abstract, the linear quadratic model (23) has seen ubiquitous clinical adoption, being used to determine fractionation patterns, amongst other things, given its ability to predict cell survival once the α/β ratio of a tissue is known. However, the model has a poor description of the mechanistic basis for the biological variation seen in cells, despite much effort to robustly determine what the α and β parameters represent. Linked systems of rate equations, such as those used by Belov et al. (24) and Dolan et al. (25, 26), can describe the interaction of multiple repair pathways by simulating the rates of specific mechanistic steps. However, this approach lacks any description of the induced damage pattern, known to impact biological response (27–30). To incorporate this spatial dimension, Poisson statistics can be used to randomly place DSBs in a simulated cell nucleus. This methodology was, for example, by Sachs et al. (31) to investigate chromosome aberration induction after photon irradiation. However, ion irradiation has been shown to produce damages primarily along a limited number of particle tracks (32), making this description unsuitable for investigating proton- or carbon-ion-therapy.

Modelling of these modalities can instead consider damages to be placed stochastically along particle tracks through the nucleus. This approach allows comparison of ion and photon biological effects such as in work by Ballarini et al. [BIophysical ANalysis of Cell death and chromosome Aberrations (BIANCA)] (33) and McMahon et al. [Mechanistic DNA Repair and Survival (MEDRAS)] (34–36). These models have shown a capability to account for cell specific responses by considering differences in damage induction. The BIANCA model has shown good capability to be fit to specific cell lines by scaling the number of critical lesions induced (37). The MEDRAS model has shown similar capability by instead considering the genome size and chromosome number (34). By additionally including some description of the individual repair pathways, MEDRAS can reproduce the effect of repair deficiency (36). The local effect model (LEM) developed by Scholz et al. (38) and built upon by Elsasser et al. (39) shows how consideration of the spatial proximity of lesions,

both through SSB combining to form DSB and overall DSB proximity, could be related to biological response, proposing that it could be the defining feature of LET dependent biological effect. Using this approach, the LEM and microdosimetric kinetic model (MKM) (40), which largely follows the same principles, have shown good ability to predict cell survival for carbon-ion therapy. Because of these demonstrated capabilities both the LEM and MKM have received clinical acceptance for carbon-ion therapy in Germany and Japan (41).

However, these models neither include descriptions of specific mechanistic steps in the repair processes, nor explicit descriptions of DSB end mobility. A less abstract approach to the inclusion of the spatial distribution of DSBs is to use Monte Carlo track structure simulations, such as the Geant4-DNA (42–44) extension used in work by Henthorn et al. (45), TOPAS-nBio (46, 47), or the PARTRAC software developed by Friedland et al. (48). Further work by Friedland et al. (49, 50) and Henthorn and Warmenhoven et al. [DNA Mechanistic Repair Simulator (DaMaRiS)] (51, 52) considers the implications of this highest level of detail by linking the detailed track structure derived DNA damage to mechanistic models of DNA repair. PARTRAC, being one of the least abstract models alongside DaMaRiS, has seen extensive scientific development up to incorporating predictions of chromosome aberrations (53).

By reducing the level of abstraction, models can more explicitly incorporate differences in radiation and biological conditions, moving from a descriptive to a predictive capacity. However, these mechanistic models suffer from their own specificity, in that their accuracy is limited by our sparse knowledge of the DNA repair pathways, the complexity of the system formed by all the interacting molecules, and the challenges associated with implementing models of such systems. Additionally, the propagation of errors through the increased number of model parameters results in a larger uncertainty in behavior if not carefully accounted for. Therefore, more pragmatic descriptive approaches have been preferred in the clinic.

The above-discussed models all contain assumptions about the underlying physical and biological processes. As can be seen, different groups have chosen different starting assumptions on which to build their models to reduce the complexity of the problem being studied. These assumptions can have both direct consequences as well as implicit impacts on subsequent processes; particularly when, for example, a DNA repair model is optimized on a particular DNA damage model to fit later experimental endpoints. In such a situation there may be a chain of mechanisms that compensate for assumptions in the DNA damage model when fitting predictions of the DNA repair model to observed results. Such dependencies may not be immediately obvious when investigating individual models. In this work we exploit access to multiple damage and repair models to combine them in alternative pairings. In this manner chains of compensatory mechanisms are broken. Through analysis of how these results differ from the naturally paired models such compensatory chains become easier

to identify. Further, by taking note of the magnitude of divergence that each mechanism is responsible for, such inter-comparison can highlight the sensitivity of models to these assumptions and suggest important areas for experimental investigation.

In this work we compare models previously developed by Henthorn (*45*, *54*), McMahon (*34*, *35*), McNamara (*55*), and Warmenhoven (*51*, *52*). We demonstrate that seemingly slight differences in initial assumptions regarding DNA damage induction can lead to significant differences in predicted DSBs. These differences then necessitate different responses of the DNA repair models to fit later biological endpoints. We demonstrate that, despite significant differences in the spatial range of assumed random DSB end diffusion during repair, the density dependent misrepair of DSBs emerges as a common property. However, the significant quantitative differences between rates and ranges of misrepair result in a divergence of the mechanisms predicted to be responsible for DSBs persisting to 24 hours.

METHODS

Inter-Comparison Overview

In this work we compare the behavior of three DNA damage models and two DNA repair models. These are specifically the NTH damage model (*45*), the ALM damage model, the MEDRAS damage and repair models (*34*, *35*), and the DaMaRiS repair model (*51*). The MEDRAS damage and repair models were developed together as were the NTH and DaMaRiS models. Although the ALM damage model does not have a paired repair model, similarities in model assumptions with the NTH model make DaMaRiS the most natural pairing. In this work, when referring to a combination of damage and repair models the syntax is <damage model>-<repair model>, e.g., NTH-DaMaRiS. Full details of each model's parameters can be found in the referenced work, though a table detailing the parameters used in these models and how they were determined is provided in Supplementary Table S1 (https://doi.org/10.1667/RADE-21-00147.1.S1).[3] Similarly, a short description of each model is provided below.

Model predictions were compared for a range of mono-energetic proton irradiations. To ensure an even spread across a range of proton LETs, ten mono-energetic energies were selected between 0.975 and 34 MeV, representing an LET range of 29.78 to 1.77 keV/μm and presented in Supplementary Table S2 (https://doi.org/10.1667/RADE-21-00147.1.S1). The irradiation of cell nuclei was simulated at each energy, with damages scored and stored in a standard format which both the MEDRAS and DaMaRiS repair models can parse. Similarly, the standard format ensures equal comparison of the initial damage distribution. The damages predicted by the models were investigated in terms of the total yield, average complexity, and proximity of the DSBs. The repair of each damage distribution was then simulated using both repair models, and the results of the repair models were investigated in terms of residual and misrepaired DSBs at 24 h.

Use of a Standard Format for DNA Damage

The damage format used in this work follows the conventions defined for the standard DNA damage (SDD) data format (*56*), which consists of a header containing information needed to recreate the simulation and a list containing the details of each DSB recorded. These details include the geometric position of the DSB as well as its complexity in terms of extra backbone and base damages. Within the

SDD, complexity could either be reported as a simplified total number of each damage or be stored as a detailed structure to be processed by the repair models. In this work we have elected to use the simplified total number of each damage.

The NTH DNA Damage Model

The DNA damage model published by Ingram et al. (*54*) is split into two stages [detailed in previous publications (*45*, *51*)], one to determine DSB yields and distributions, and the other to determine DSB complexity. Both stages use Geant4-DNA (10.5) track structure simulations (*44*, *57*, *58*). In the first stage, DSB positions are determined in a spherical nucleus (nominal radius 4.0 μm) centred in a larger sphere (radius 6.5 μm). The chromosome geometry in this model is informed by Hi-C measurements. Gene-gene contacts for a range of cell lines have previously been measured and made available in the literature to produce "Hi-C contact maps" (*59*). Within the nucleus, chromosome topologically associated domains are constructed as a series of spherical polymer beads, with bead sizes and positions determined by solving the Hi-C gene-gene contact maps for an IMR90 lung fibroblast cell. To assess DNA-DSB yield and distribution the nucleus is uniformly irradiated with mono-energetic protons and energy deposition events (energy and position) that occur within beads are recorded. As only a portion of the bead volume is filled with DNA, only a portion of the energy deposition events occur within the DNA. For this stage of the model, chemistry is not explicitly simulated so to compensate, physical energy deposition events are "over-accepted". This results in 14.1% of energy deposition events occurring within beads being randomly selected as energy deposition events occurring in DNA. These energy deposition events are then converted into strand breaks via a probability that varies linearly from 0 to 1 between 5–37.5 eV (*60–63*). Accepted strand breaks are then randomly assigned to strand 1 or 2 of the double helix with equal probability (*64*). Strand breaks are then clustered into DSBs by a modified DBSCAN algorithm (*65*), with the conditions that strand breaks have to be on opposing strands, within the same chromosome, and separated by 3.2 nm or less. In the second stage, DSB complexity is determined from separate simulations using a chromatin fiber model, with explicit DNA backbone and base volumes, irradiated by protons of a matching energy. Energy depositions in DNA are summed per primary proton or electron, as appropriate, and the same energy based probability is used to determine DNA damage. Geant4-DNA chemistry (*42*) is implemented within the fiber model to simulate indirect damage. Hydroxyl radicals are assigned a probability, P, of creating damage when crossing the DNA volumes (P = 0.5 for backbones, P = 0.8 for bases) (*66*). Damaged backbones on opposite strands separated by 10 base pairs or less are clustered into DSBs. Damaged bases are included if they are no more than 3 base pairs outside the ends of the DSB. DSBs that contain only two damaged backbones are classified as simple. DSBs that contain any additional damages are classified as complex. These detailed DSBs are used to populate the DSB positions determined by the cell simulation.

The ALM DNA Damage Model

Similar to the NTH damage model, the ALM model is split into stages, both based on Geant4-DNA track structure simulations. The geometry was developed by McNamara et al. (*55*) within TOPAS-nBio (*67*), a simulation framework based on Geant4-DNA. This DNA geometry is based on a knot-free fractal globule model of chromatin folding (*68*, *69*). For this, a 3D space filling Hilbert curve is generated using a recursive function that creates a basic building block of an open cube consisting of seven cylinders. The fractal pattern is made by recursively converting each cylinder to a smaller version of the original starting pattern forming a continuous curve. The 3D space filling Hilbert cube is "cut" to fill the full spherical nucleus of 4.0 μm radius. The final geometry contains 327,637 cylinders, each with a diameter of 30.8 nm and a length of 161 nm. These cylinders represent a DNA fiber of 90 nucleosomes. Each nucleosome is comprised of a cylindrical histone protein with diameter of 6.5 nm and length of 5.7 nm, wrapped with two turns of the DNA double helix, containing a total of 200 base pairs (*70*). The DNA double helix strands are composed of two separate strands built from the union of spheres representing the sugar-phosphate backbone

J_ID: RARE Date: 17-October-23 Page: 4 Total Pages: 15

Page proofs and all forms must be returned with 72 hours of receipt.

0 WARMENHOVEN ET AL.

and the base. The sugar-phosphate backbone of the DNA has a total diameter of 2.16 nm and the DNA base has a diameter of 0.34 nm.

The first stage of the ALM damage model irradiates the 3D space filling Hilbert curve consisting of empty cylinders with a beam of mono-energetic particles. A phase-space, that is a list of particles with their position, 4-momentum, energy, etc., is scored on each cylinder surface along with additional information specific to the geometry, e.g., chromatin fiber number. The position and orientation of the cylinder is also saved, for reorientation in the whole nucleus after stage two. For stage two, a single fiber containing the full DNA geometry as described above is irradiated using the phase-spaces from stage one, breaking the simulations down per particle. These simulations are run using the default TOPAS-nBio physics lists (71) and chemistry implementations for TOPAS-nBio version 1.0-beta and TOPAS version 3.2 (72). The TOPAS-nBio physics module is based on the default Geant4-DNA constructor. Energy deposition events in the DNA structure are scored as strand breaks using a linear probability model with bounds of 5–37.5 eV. Chemical species that interact with histones are assumed to be scavenged. Hydroxyl radicals are assumed a 50% probability of creating damage when interacting with the DNA components. All other settings for stage two, apart from the geometry, are consistent with those used in the NTH damage model. The final output of stage two is analyzed in Matlab, combining the individual runs and reorienting the final scored values to the original nucleus before outputting the data using the SDD format (56).

The MEDRAS Damage Model

In the DNA response model published by McMahon et al. (34, 35), the probability of a DNA damage event occurring within a nuclear volume depends linearly on the density of DNA and total energy deposited within it. From fitting to experimental data E_{DSB}, the energy required to create an average of 1 DSB, can be determined based on an assumed yield of 35 DSB/Gy/cell and the nucleus volume. For the 4-μm radius cells used in this work, the corresponding energy is 47.7 keV. Importantly, this assumption means that the absolute yield of DSBs depends only on dose and is independent of LET. Damage complexity is assigned by random sampling, with a complex DSB probability determined by the ratio of slow and fast DSB repair as fit to experimental measurements of DNA repair in previous work (34). Individual proton tracks were directed along the z-axis at random radial positions within the nucleus. DSBs per track were sampled from a Poisson distribution with a mean determined by the track's LET, distance travelled through the cell, and E_{DSB}. The radial distance between the track core and each DSB was obtained by sampling from cumulative radial energy distributions pre-calculated for different proton energies (35). The total number of tracks was also Poisson-distributed, based on the fluence required to give a particular dose.

The MEDRAS Repair Model

The MEDRAS repair model makes use of a simple probabilistic Monte Carlo approach to describe misrepair. Starting from a distribution of DSBs within the nucleus, each DSB is modelled as a pair of free DNA ends in close spatial proximity. As the cell repairs DSBs, each free end has a probability of interacting with every other free end in the nucleus with a rate given by $\lambda e^{-\frac{r^2}{2\sigma^2}}$, where λ is a constant determining the rate of repair, r is the separation between the two free ends and σ is a parameter governing the interaction range of repair. This distance-dependent factor will be approximately 1 for correct repair of the two ends created from the same DSB, as their separation is much less than σ. For other DSBs this factor can be close to 1 if they occur in close proximity to the DSB considered, falling to 0 for distant DSBs. Parameter values have been obtained by fitting to experimental data (34). In particular, σ has a value of $0.0428R$, where R is the nuclear radius, giving $\sigma = 171.2$ nm for normal human cells with $R = 4.0$ μm as described above. Repair events are then identified as either correct repair (when two matching free ends from a single DSB rejoin) or misrepair (when two ends from different DSBs rejoin).

This means the rate of correct repair is a constant (as there is only one correct matching end), while the rate of misrepair can be increased

through either an increase in dose (creating more DSBs) or LET (creating more densely spaced DSBs). This will in turn lead to increases in the probability of misrepair. Residual DSBs can be estimated based on the number of free DSB ends at a given timepoint, which increases with increasing misrepair as isolated DSB ends can be formed with no nearby free ends with which to repair. For this simulation, a single repair pathway reflecting c-NHEJ is modelled, as this is the primary repair pathway in G1 phase nuclei, as simulated in the damage models.

The DaMaRiS Repair Model

DaMaRiS is a mechanistic Monte Carlo repair simulation (52). In this work the c-NHEJ pathway is simulated which is the dominant pathway in the G1 cell cycle stage. DSBs are represented as two independent ends in a simple spherical geometry that move by sub-diffusion, following data on DNA mobility found in the literature (73, 74). DSBs progress along the repair process by acquiring repair proteins through stochastic time constant based state changes. DSB ends in the appropriate state and within a defined interaction range (25 nm) can form synaptic complexes. Synaptic complexes can either fail, reverting both ends to their initial state (75, 76), or progress to final ligation steps including the processing of additional complexities. Once ligated, DSBs are classified as fixed. Residual DSBs are scored as the initial DSBs minus the DSBs classified as fixed. This represents DSB ends and synaptic complexes with active repair proteins capable of producing foci. Synaptic complexes and fixed DSBs that contain ends not originally from the same initial DSB are scored as misrepaired. Synaptic complexes at 24 h are counted as contributing to stable misrepairs as they are unlikely to dissociate. Pre-synaptic recruitment kinetics (76–79), rate of formation, failure, and stabilization of synaptic complexes (76, 80–83), variation of residual DSBs with LET (84), and repair kinetics (84) are fitted to data found in the literature.

RESULTS

Figure 1 presents the DSB yields and average complexities obtained from the three damage models. MEDRAS shows a constant ≈ 35 DSB/Gy/cell and a constant proportion of ~ 0.7 complex DSBs for each simple DSB, independent of radiation type or LET. In contrast, the NTH model predicts a linear trend of increasing DSB yield, starting at ≈ 32 DSB/Gy/cell for 1.8 keV/μm proton irradiations and predicting ≈ 70 DSBs/Gy/cell for 29.8 keV/μm proton irradiations. Complexity is also predicted to increase linearly with LET, going from ≈ 0.4 complex DSBs for every simple DSB to an almost equal split over the LET range investigated. The ALM model predicts a similar trend in DSB complexity to the NTH model, only differing substantially at the highest LET of 29.8 keV/μm where a sharp decrease in complexity is predicted. In contrast, the predicted DSB yields of the ALM model are substantially different from both MEDRAS and the NTH model. DSB yields starts off similar for all three models, after which the ALM model shows a steep increase in DSB yield with LET, peaking at 20.6 keV/μm with 85 DSB/Gy/cell and then decreasing gradually to match the predicted 70 DSB/Gy/cell of the NTH model at 29.8 keV/μm. Similar trends in the coefficients of variation (CoV) can be seen for the MEDRAS and NTH models, showing increasing variation in the number of DSBs per cell with increasing LET due to the reducing number of particle tracks per cell. The ALM model shows a flat trend in CoV with LET.

F1

Figure 2 compares the initial spatial distribution of DSBs between the damage models for single proton tracks. In this

F2

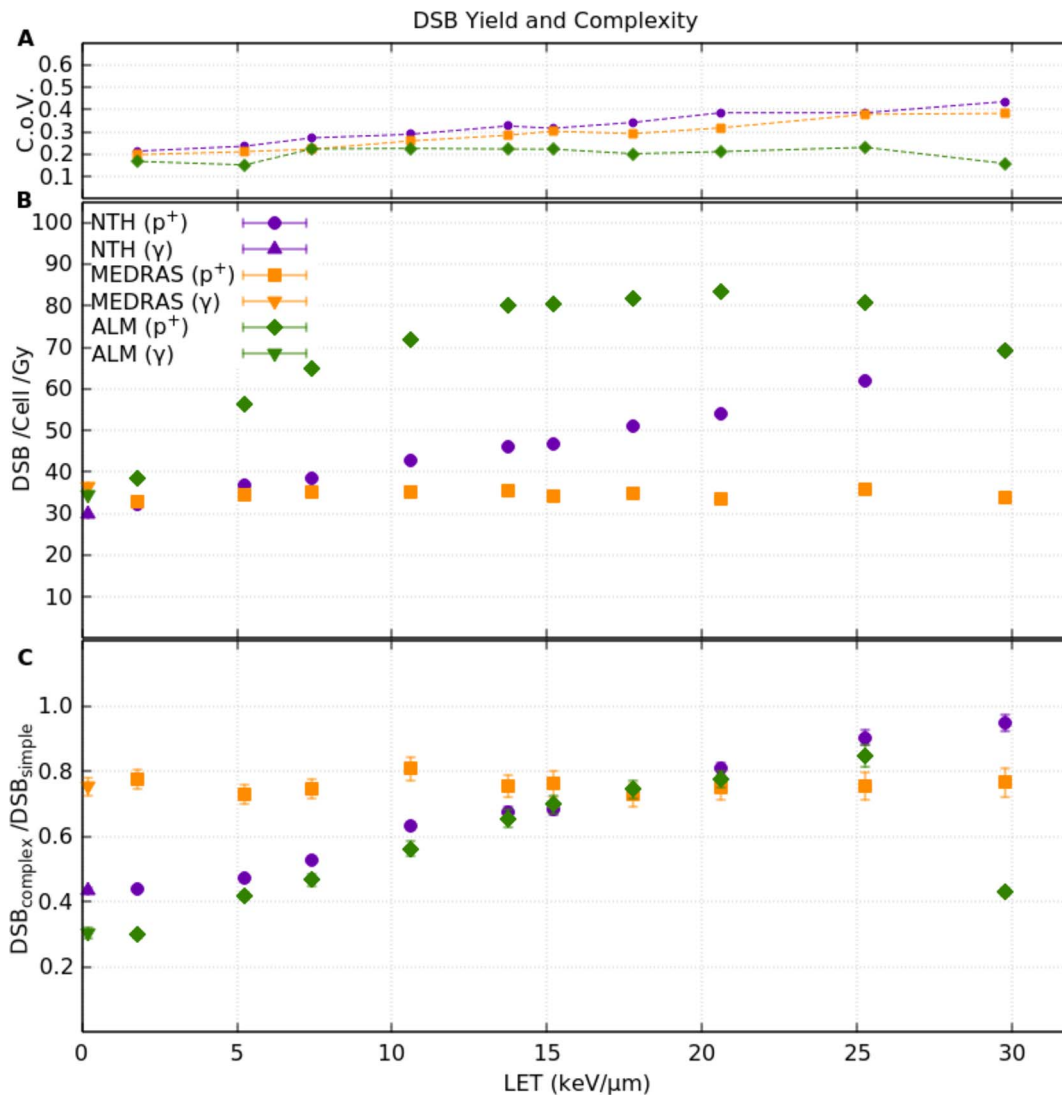Page proofs and all forms must be returned with 72 hours of receipt.

FIG. 1. Panel A: The coefficient of variation for the predicted yield of DSBs per cell per Gy for each model. Panel B: Average yield of initial DSBs per cell per Gy predicted by the damage models for a range of proton LET and Co-60 photons (see Supplementary Table S2; https://doi.org/10.1667/RADE-21-00147.1.S1). For all models, yields are for a spherical nucleus irradiated with 1 Gy of mono-energetic radiation, plotted against corresponding LET (calculated in a 1 μm thick water slab). NTH data is from 400 repeats of 1 Gy exposure, MEDRAS data from 100 repeats, and ALM from 100 repeats, making the standard error in the mean for all points too small to be visible. Panel C: The average complexity is plotted as the ratio of complex breaks to simple breaks at each LET in each model. Simple breaks are defined as DSBs involving only two backbone breaks, and complex breaks as involving two backbone breaks with any additional number of damages (extra backbones or bases included in the damage cluster). Error bars represent the standard error in the mean and are too small to be visible for most datapoints.

case the proton started at the center of one face of the nucleus and was directed towards its center, covering the maximum thickness. Although the DSB density of individual tracks increases with LET for all models, different trends are seen. While MEDRAS predicts a linear relationship between DSB density along tracks and LET, NTH shows a greater induction of damage at high LETs that has been fit here with a quadratic relationship. The ALM model appears to follow a more complex trend, being initially linear up to 25 keV then falling at the highest LET (here fit as a cubic polynomial). MEDRAS and the NTH damage models agree relatively well at LETs up to ~10 keV/μm, with predicted DSB density along the

tracks starting to diverge at the ≈10.6 keV/μm data point. Above this LET, the NTH damage model predicts a more rapid increase, reaching 0.4 DSB/track/μm at ≈15.2 keV/μm, which is not reached in MEDRAS untill ≈20.6 keV/μm. Over the LET range investigated the ALM model predicts consistently higher DSB density along the proton tracks appart from at the lowest LET, where it agrees with the other models, and at the highest LET, where it predicts lower DSBs than for an LET of 25.4 keV/μm and agrees with the NTH model.

The radial dependence of these DSBs (Fig. 2B) in all models follows an S-shaped curve. The proportion of

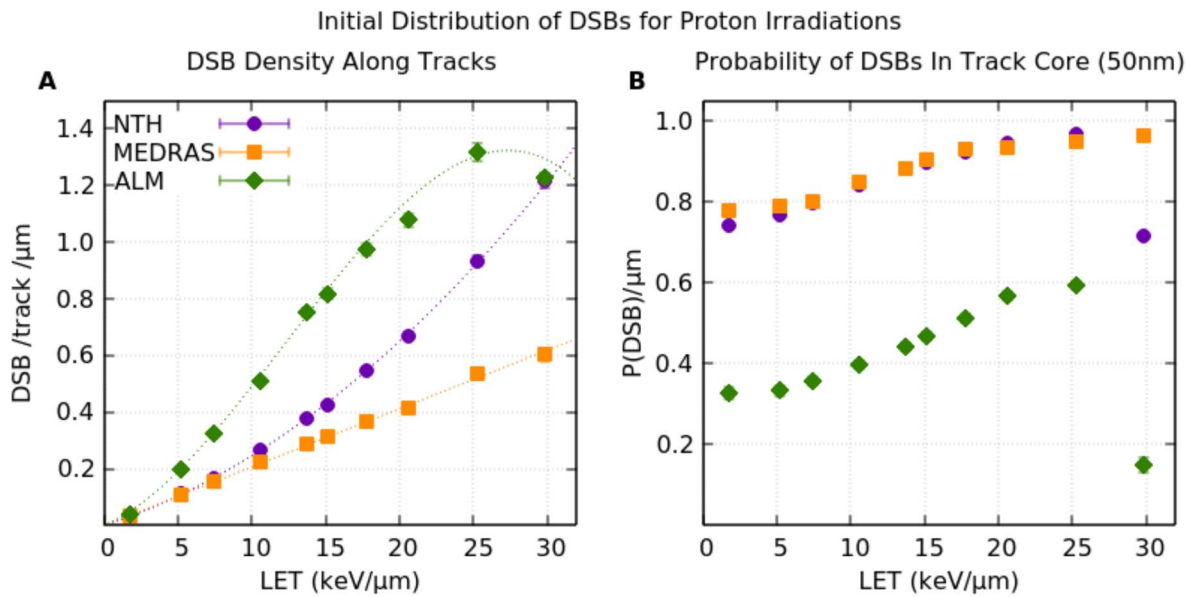0   WARMENHOVEN ET AL.

Initial Distribution of DSBs for Proton Irradiations

FIG. 2. Panel A: Average yield of DSBs per track per μm predicted by the damage models for protons; simulated by single-track irradiations. Dashed lines are fitted equations for each model. Panel B: The probability of these DSBs being generated inside the track core, arbitrarily defined to be of 50 nm radius. NTH data is from ~180,000 repeats of single proton tracks, MEDRAS data from ~3,000 repeats, and ALM data from ~2,000 repeats, making the standard error in the mean for most points too small to be visible.

DSBs created inside the 50 nm track core in the NTH and MEDRAS models start at ≈0.8 at low LET, rising to near unity by 25.3 keV/μm. While showing a similar trend, the ALM model predicts a smaller proportion of DSBs within the track core with a ratio of ≈0.3 at low LET, rising to ≈0.6 at 25.3 keV/μm. While the MEDRAS model continues at near unity past 25.3 keV/μm, both the NTH and ALM models predict a sharp drop in the number of DSBs contained in the 50 nm core by 29.8 keV/μm, reaching 0.7 and 0.1, respectively. This is due to both models using track structure simulations that result in the proton tracks deflecting out of the geometric cylinder used to calculate this metric, making it an artifact of our measurement technique as the "track core" ceases to be well-defined.

F3   Figure 3 shows the biological endpoints of residual DSBs and misrepaired DSBs at 24 h postirradiation for different combinations of damage and repair models. In Fig. 3A the MEDRAS and NTH-DaMaRiS models show similar linear trends in residual DSBs with LET. Although there is a systematic offset between the two models, these linear trends are comparable to literature results of 53BP1 foci (84). The ALM-DaMaRiS model follows a similar trend as that seen for the DSB yields predicted by the ALM model in Fig. 1B. The comparison to Fig. 1B is reinforced by considering the relationship between DSB yields as predicted by the NTH and ALM models, and comparing that to predicted residual DSBs by the NTH-DaMaRiS and ALM-DaMaRiS model pairings.

Both MEDRAS and the NTH-DaMaRiS model combinations show comparable yields of misrepaired DSBs in Fig. 3C. Their behavior differs in that MEDRAS displays a linearly increasing yield of misrepair with LET, and the NTH-DaMaRiS model shows an exponential trend. When applying the DaMaRiS repair model to the ALM damage model the behavior can again be well described by a cubic relationship. When using

the SDD to connect models that were not developed together, significantly different predictions for both residual and misrepaired DSBs are produced. The NTH-MEDRAS combination results in a steep, quadratic, dependence on LET for both residual and misrepaired DSBs. The MEDRAS-DaMaRiS combination shows a flat response for residual DSBs and only a very small linear increase of misrepair yield across the LET range. Similar to the NTH-MEDRAS repair, the ALM-MEDRAS combination results in a marked increase in both the predicted residual DSBs and misrepaired DSBs.

Comparing the yields for these two biological endpoints reveals that the MEDRAS model predicts a higher yield of misrepaired DSBs than residuals across the range of LET investigated. On the other hand, the NTH-DaMaRiS model predicts the opposite, with yields of residual DSBs greater than misrepaired DSBs up to an LET of 25.3 keV/μm. The ALM-DaMaRiS model predicts that this cross over will happen at 10.6 keV/μm.

To explain the behavior of the models with respect to misrepaired DSB yields, we investigated the interaction of DSBs with incorrect partners in Fig. 4. For DaMaRiS, two DSBs   F4 were placed at specified separations and simulations run to determine the probability of misrepair. For MEDRAS the equation governing the interaction probability for two DSBs was solved. Both DaMaRiS and MEDRAS exhibit sigmoidal interaction probability curves, favoring interaction of nearby DSBs over distant DSBs. At 0 nm separation the misrepair probability for MEDRAS is 0.67. This is because in a system of two DSBs each DSB end has two possible incorrect partners and one possible correct partner, with the first interaction determining the possible correct/incorrect state of the remaining ends. Due to the inclusion of sub-diffusive motion in DaMaRiS DSB ends can become isolated and therefore not
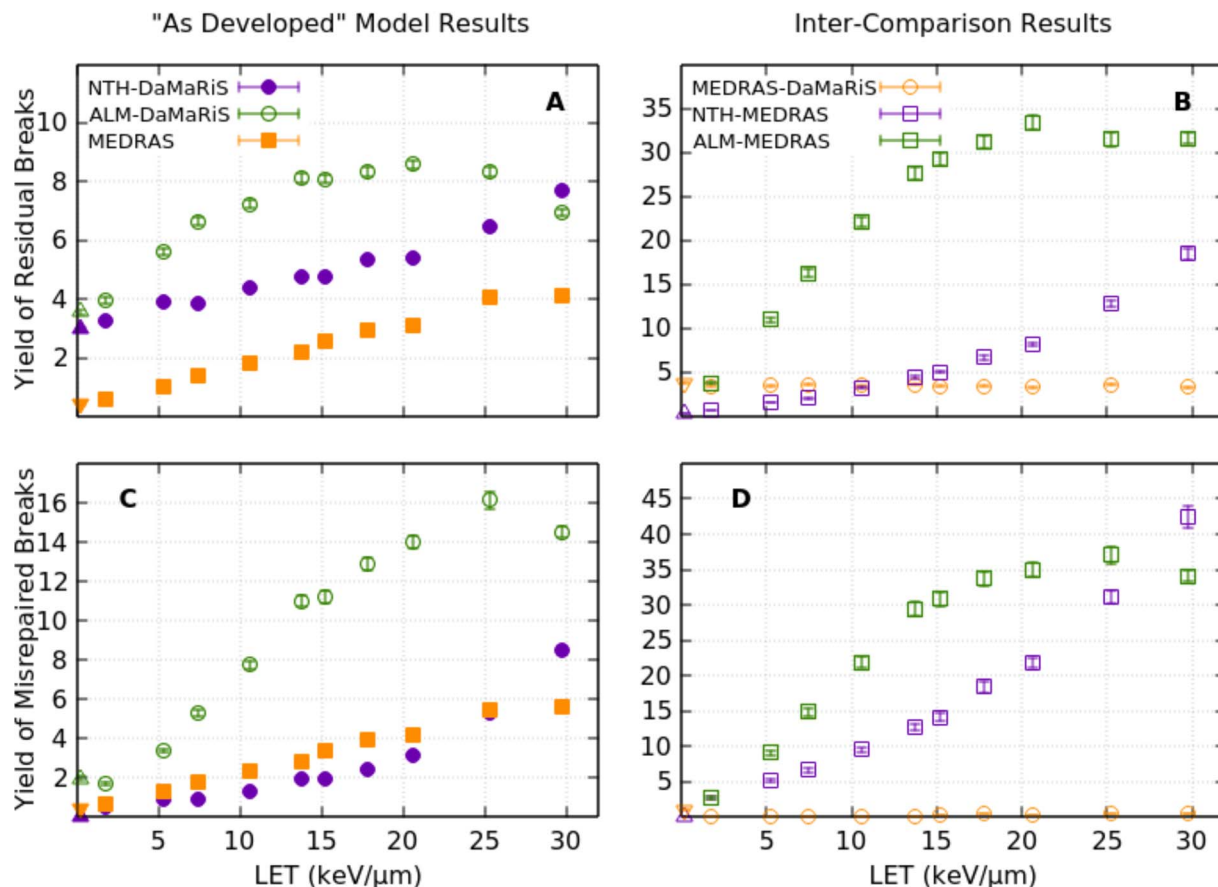
FIG. 3. Yield of (panel A) residual and (panel B) misrepaired breaks at 24 h after 1 Gy dose in a spherical nucleus for a range of proton LET and photons (0.2 keV/μm). Results from previously discussed damage models were used as input to the DaMaRiS and MEDRAS repair models. Filled symbols represent results of "matched" model combinations whose parameters were fit together (*34*, *35*, *51*). Open symbols represent unpaired model combinations. Photon data are shown as triangles for repair by DaMaRiS and inverted triangles for repair by MEDRAS. Errors are standard error in mean for 500 repeats with the DaMaRiS model, and 500 repeats with the MEDRAS repair model.

repaired. For this reason, the misrepair probability at 0 nm is not 0.67 but instead 0.6. The models also differ in interaction range, with DaMaRiS having an interaction range with half-width half-maximum (HWHM) of 26.15 nm, and a negligible interaction probability at separations >100 nm. In contrast, MEDRAS has a similarly shaped function but an interaction range an order of magnitude larger at 285.06 nm (note this is larger than the parameter σ for individual DSB ends, as each additional DSB contributes two potential ends with which misrepair can occur, while there is only one correct repair partner). When applied to similar damage patterns the narrower interaction range of DaMaRiS should result in a higher rate of correct DSB end pairing than the wider interaction curve of MEDRAS, possibly explaining the behavior observed in Fig. 3D.

DSB clustering was quantified by calculating the average number of DSBs within a given range from each DSB in a simulated 1 Gy dose. The radii used to analyze the damage models were set to the HWHM of the interaction ranges from their partner repair model. Again, although the ALM damage model doesn't have a paired repair model, DaMaRiS was

used as the most natural pairing due to its high damage density. MEDRAS and the ALM model show a linear increase in neighboring DSBs across the LET range whereas the NTH damage model shows an exponential increase. It should be noted that these trends do not reflect the relations seen in DSB density along the track from Fig. 2A.

Comparing the average number of neighboring DSBs to the misrepair probability for a given DSB produces initially linear trends for all three model combinations. Misrepair probability can therefore be said to be dominated by the number of potential incorrect partners available to each DSB end within the locality determined by the repair model range. A similar concept has been explicitly used in analytic formulations of the MEDRAS model, where the sum of the DSB interaction rates for an average exposure condition is used to calculate misrepair rates (*34*). The simple sum of DSBs within the HWHM provides an approximation to this more complex calculation.

DISCUSSION

This work compares models of DNA damage and repair, each with differing levels of model complexity. From this

Page proofs and all forms must be returned with 72 hours of receipt.
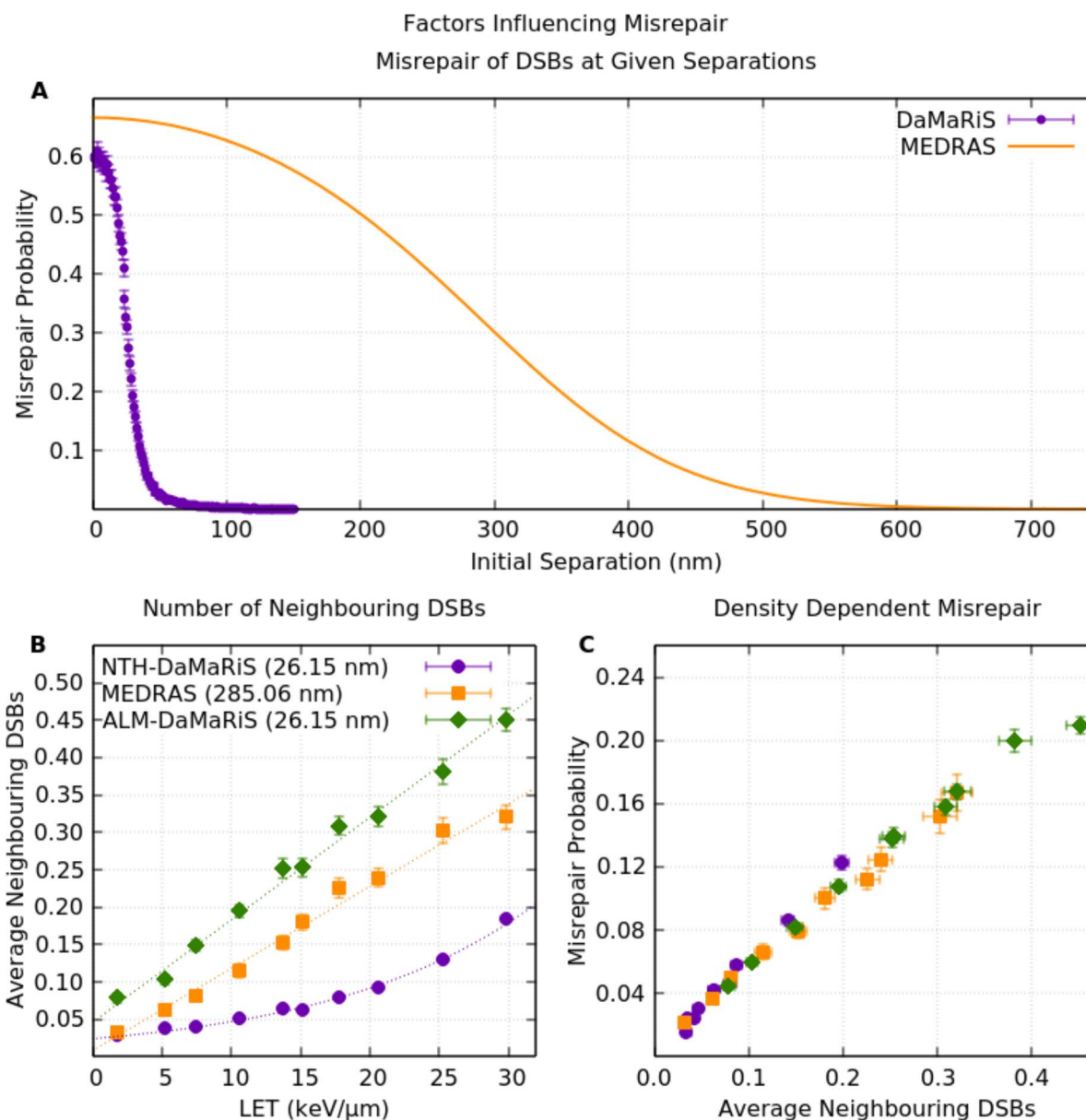
WARMENHOVEN ET AL.

FIG. 4. Panel A: The probability of an interaction leading to misrepair for a pair of DSBs as a function of initial separation. The solid line is an analytical plot of the function used by MEDRAS to determine interaction of two separate DSBs. Filled circles are average results from 1,000 repeats of DaMaRiS with associated standard error in the mean. Panel B: For 1 Gy irradiations, taking into account the HWHM of this characteristic interaction range, the average number of neighboring DSBs for any given DSB within 26.15 nm for the NTH damage model and within 285.06 nm for MEDRAS is plotted with proton LET. Dashed lines show a linear correlation for MEDRAS and ALM, and an exponential correlation for the NTH damage model, equations and parameters for which are shown in Supplementary Table S3 (https://doi.org/10.1667/RADE-21-00147.1.S1). Standard error in the mean is too small to be visible in most cases. Panel C: The misrepair probability can be correlated with the average number of neighbors for both MEDRAS and DaMaRiS repair. Dashed lines show the fitted correlations with parameters given in Supplementary Table S3. Errors are standard error in mean for 500 repeats with DaMaRiS, and 500 repeats with MEDRAS.

comparison we investigate the effect of incorporating full Monte Carlo track structure, detailed modelling of DNA geometries, and detailed biological repair pathway simulations. Furthermore, we explore the different biological assumptions these models make to arrive at similar experimentally observable outcomes. Simulations were also done on photon irradiations, however, because their behavior does not deviate from what is expected given the trends of the proton data in our models, the discussion is focused on results from proton irradiation. Similarly, we would expect the general mechanisms

discussed in this work to hold for simulations using other particles in these models.

This manuscript shows how seemingly small differences in assumptions in MEDRAS and the NTH model led to significantly different predictions in initial damage yield. Specifically, while MEDRAS places DSBs proportional to the energy deposited in the nuclear volume, the NTH damage model could be considered to place SSBs based on single energy deposition events which are then clustered into DSBs. When considering one proton track crossing the nucleus, Fig. 2B

shows that the DSBs in both models are predominantly contained within 50 nm of the proton track and as such we can consider the models to be placing the above-mentioned damages along these tracks. For MEDRAS, therefore, a doubling of energy due to an increase of proton LET necessarily results in a doubling of the number of DSBs along the track, and this linear relationship can be seen in Fig. 2A. Conversely, the NTH damage model shows a quadratic increase in Fig. 2A because with each additional SSB there is less track length available where a new energy deposition is genomically isolated enough from existing SSBs to avoid being clustered into a new DSB. This will also increase the conversion of simple DSBs into complex DSBs by the creation of additional nearby backbone or base damages, resulting in the behavior seen in Fig. 1C for the NTH model.

Explicit modelling of the DNA and the chemical stage in the ALM model introduces stricter geometric constraints on where DNA damage can occur. In the NTH model, any energy deposition event occurring within a Hi-C bead and less than 3.2 nm from an existing SSB has the possibility to result in a DSB. In the ALM model however, only a thin fiber of DNA adjacent to a SSB becomes sensitive to energy depositions that would convert the damage site into a DSB. Additionally, whereas in the NTH model DSBs can be created proximal to each other in any direction, DSBs in the ALM model can only be proximal if they are created along the geometry of the DNA strand. Figure 1 shows that at higher LET these stricter limits on where DSBs can be formed interact with a higher density of energy deposition events to reduce the total yield of DSBs. Furthermore, in the ALM model it is possible for incident protons to pass some distance from DNA fibers and thus not be able to create any DSBs in their immediate vicinity. These factors combine to create more radially dispersed DSBs as shown in Fig. 2B. Considering only LET up to 10.6 keV/μm, DSBs in the ALM model are 2.6 times less likely to be created within the track core than those of the NTH or MEDRAS models. Given the 2.5 times higher linear DSB density of the ALM model shown in Fig. 2A, it is tempting to hypothesize that this is driven mainly by the additional DSBs that are created away from the path of the track. However, as can be seen later, this explanation is not enough to unambiguously define the model behavior on the scales that are relevant to the repair models. Figure 4B shows that there is an increase in highly correlated DSBs created within 26.15 nm of each other over that of even the NTH model, which contributes to the increased density in Fig. 2A.

To deliver a 1 Gy dose to the nucleus, a 4-μm radius sphere of water, requires 1,672.3 keV of energy deposited. Therefore, the total track length of a particle required to pass through the nucleus scales proportionally as 1,672.3/LET. Applying this proportionality to Fig. 2A results in an LET-independent number of DSBs for MEDRAS, a linear relationship between DSB and LET for the NTH damage model, and a quadratic relationship for the ALM damage model all of which is consistent with the data shown in Fig. 1B.

Despite the differences in underlying assumptions for MEDRAS and the NTH model, Fig. 3A and C show that both display a similar trend in predicted residual DSBs at 24 h and a similar predicted yield of misrepaired DSBs. The similar yields of misrepaired DSBs in MEDRAS and NTH-DaMaRiS are remarkable for two reasons: Firstly, while the MEDRAS model was fit to experimental data on misrepair of X-ray irradiations, the NTH-DaMaRiS model combination was not, and the LET dependence of misrepair is instead an emergent property for both models. Secondly, there is a large difference between the two models in the complexity of the process which leads to misrepaired DSBs. Both models assume that misrepair occurs through the pairwise interaction of incorrect partner DSB ends. MEDRAS describes both the interaction and repair of DSB ends in a single step with a single probability depending only on their initial position. DaMaRiS contains a detailed mechanistic description of the processes which convert DSB ends to fixed, as well as a mechanistic description of the random sub-diffusive motion of individual DSB ends. This large difference in model complexity, and therefore simulation time, results in a difference in misrepair yield of less than 3 DSB/Gy/cell across the LET range investigated. The fact that these two independently developed, structurally different models arrive at similar predictions for misrepair yield, where only MEDRAS was fitted against experimental data related to this endpoint, implies that random undirected rejoining of DSB ends in combination with the density of DSBs could be a driving factor in elevated misrepair at high LETs.

As DSB density is the driving factor in misrepair, Fig. 2A is expected to be predictive of Fig. 3C and D, which mostly holds accurate for Fig. 3C. The slight difference in trends of misrepair with LET between Figs. 2A and 3C could be explained if a missing mechanism that is linearly dependent on LET is driving up the yield in MEDRAS and ALM-DaMaRiS. However, the relationship breaks down for Fig. 3D, where the similarity in the predicted yield between MEDRAS and DaMaRiS is destroyed. Using the 5.3 keV/μm data point from Fig. 2A as an illustrative example, predicted damage from MEDRAS is approximately the same density as from the NTH model, whereas ALM damage is expected to be roughly double the density. While the relationship between NTH and ALM damage is maintained in Fig. 3D, the yield of misrepaired DSBs in the MEDRAS-DaMaRiS model combination is almost non-existent; a prediction which cannot be explained by Fig. 2A.

To explain this behavior the damage models must instead be analyzed on a smaller scale. While Fig. 2A suggests comparable DSB densities for both MEDRAS and the NTH model, Fig. 4B shows that the nanoscale distributions of DSBs are very different. When analyzed on a scale informed by Fig. 4A, the NTH and ALM models produce comparable numbers of DSBs within a radius of 26.15 nm of each other as MEDRAS does in a radius of 285.06 nm. This is likely because the NTH and ALM models are full track structure simulations, enabling them to reflect the potential for damage
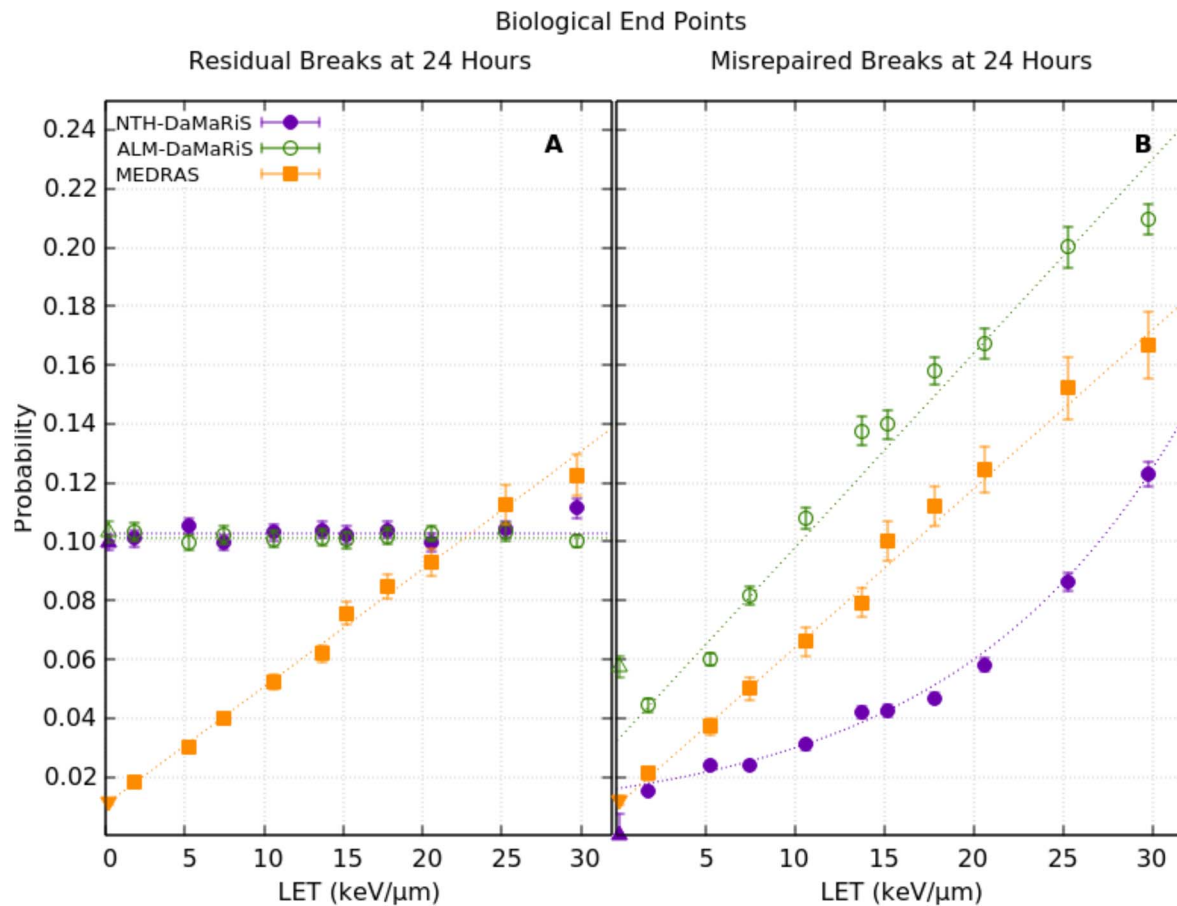
0   WARMENHOVEN ET AL.

Biological End Points

FIG. 5. Residual (panel A) and misrepaired (panel B) breaks at 24 h as a fraction of initial DSB yield after a 1 Gy dose in a spherical nucleus for a range of proton LET and Co-60 photons (0.2 keV/μm). Photon damages are shown as triangles. Errors are standard error in mean for 500 repeats with both the Warmenhoven and McMahon repair models.

to be correlated due to, for example, creation by the same secondary electron. Figure 4C shows that analyzing misrepair probability in terms of neighboring DSBs, on a scale informed by the specific repair models, harmonizes the response of the repair models to DSB density. If this misrepair probability is expressed relative to LET and applied to the initial yields of DSBs from Fig. 1B then the predictions in Fig. 3C are very well matched, as shown in Supplementary Fig. S1 (https://doi.org/10.1667/RADE-21-00147.1.S1).

This inter-comparative work therefore highlights the importance of considering DNA damage densities on the scale of the DNA helix (tens to a few hundred nm) rather than on the scale of the whole nucleus; in both the effect on overall damage induced (Fig. 1) and its subsequent impact on repair fidelity (Fig. 3).

By normalizing the results shown in Fig. 3 to the initial number of DSBs, shown in Fig. 5, we can deduce the mechanisms driving residual DSB probabilities in the models. MEDRAS has a linearly increasing probability of residual damage with LET. This behavior arises due to MEDRAS explicitly simulating repair rates which are greatest for adjacent DSBs, reducing as the separation increases. When a misrepair event occurs between ends from two DSBs, the other end of each DSB becomes relatively isolated and its

rate of repair decreases dramatically. As a result, the yield of residual DSBs (gradient = $(4.0 \pm 0.1) \times 10^{-3}$ (keV/μm)$^{-1}$, intercept = $(10.6 \pm 0.9) \times 10^{-3}$) is closely correlated with the yield of misrepaired DSBs (gradient = $(5.4 \pm 0.2) \times 10^{-3}$ (keV/μm)$^{-1}$, intercept = $(10 \pm 2) \times 10^{-3}$). The difference in gradients arises due to DSBs where both ends have misrepaired rather than one becoming isolated. Therefore, the MEDRAS repair model suggests that variation in residual DSBs with LET is due to a change in the spatial clustering of initial damages.

DaMaRiS predicts a constant probability for residuals across the LET range ($(10.3 \pm 0.1) \times 10^{-2}$ for NTH, $(10.15 \pm 0.04) \times 10^{-3}$ for ALM); ruling out a similar dependence on misrepair. From Fig. 4A it can be seen that, contrary to MEDRAS, only very proximal DSBs can misrepair in DaMaRiS. Therefore, the remaining DSB ends from misrepair events are likely to be very proximal and are likely to be resolved with each other unless they can escape proximity. The probability of misrepair is therefore predominantly a function of the mobility of the DSB ends, which is invariant with LET. Within the model, neither the number of nearby DSBs nor the inherent complexity of the DSB affects its mobility. As such, the yield of residual DSBs in Fig. 3A when applied to the NTH or ALM damage

F5

models reflects that of the initial yield of DSBs in Fig. 1B. The linearly increasing yield of initial DSBs for the NTH damage model therefore results in a similar trend in biological endpoint to MEDRAS, via an entirely different mechanism.

This inter-comparative work therefore highlights the importance of considering DNA mobility, particularly on the scale of DSB ends. The distinct implementations of DSB mobility by the repair models is enough to cause a significant change in the proposed mechanism responsible for residual DSBs.

However, these results seem to suggest that the fully mechanistic description of the repair pathway itself is not necessary to determine the likelihood of misrepair. Furthermore, both models can produce reasonable predictions of various biological endpoints with DNA damage complexity playing an insignificant role. This may be due to DSB complexity being highly correlated with parameters such as DSB density, meaning that it is not feasible to quantify the role of damage complexity independently simply by varying LET. Additionally, and perhaps more likely, the models and endpoints investigated here may not include sufficient detail to accurately determine the influence of damage complexity, highlighting a key area for improvement of the models and simulation endpoints. However, to include this added detail, additional biological experiments are required to provide the necessary fitting data to rationally expand these models. For example, it would be of great benefit to have additional data on repair protein recruitment and recovery as well as repair kinetics for cells challenged with controlled break structures.

The requirement for careful, step by step, experimentally driven expansion of these models is made even clearer when the results thus far are summarized and considered together. The damage models in this work assume the same method for inducing DNA DSBs but apply it at slightly different scales, resulting in significantly different predictions. Despite this, both repair models show the same DSB density dependent misrepair which arises due to assumed random migration of DSB ends. The exact implementation of this mobility has a determining and divergent impact on the suggested mechanism, but importantly not the overall yield of residual DSBs. This highlights how models which produce similar final results can differ dramatically in intermediate predictions such as initial DSB yield or the ranges over which misrepair can occur and underlines the necessity of combining such in silico work with experimental data at all stages of the radiation response. Supplementary Table S4 (https://doi.org/10.1667/RADE-21-00147.1.S1) summarizes and compares the trends observed in the models considered in this work, and highlights what difficulties there are in establishing the experimental ground truth.

From a clinical perspective, the probabilities in Fig. 5 can be applied to a dose map where LET has been scored, as has been done in a proof of principle for the NTH-DaMaRiS combination (*85*). This would result in a probability map for the two biologically relevant endpoints, misrepair and residual DSBs, considered in this work. Comparison between the

resultant misrepair and residual maps can then alert us if there is a significant difference predicted by assuming one or the other mechanism as proposed by the different models. From Fig. 5 it can already be seen that the MEDRAS-MEDRAS model always predicts greater misrepair yield than residual DSB yield, whereas the NTH-DaMaRiS model predicts more residual DSBs than misrepaired DSBs for LET up to $\sim$10 keV/μm.

CONCLUSION

We have shown how comparative work, facilitated by adoption of the SDD, has allowed us to explore underlying differences in mechanistic models due to assumptions made to account for a lack of experimental data. We have highlighted, through analysis of both residual damage and misrepair of DNA, the importance of considering DNA damage distributions on the nanoscale. We have also shown, through investigation of residual DSBs, how important the consideration of DSB end motion is.

Clinical implementation of biological outcome modelling is desirable but, currently, requires simplified models. However, this work shows that such simplification should be approached with caution. Models can produce similar final results despite dramatically different intermediate predictions, which can result in unknown behaviors if extrapolating to situations not explicitly fit to. This suggests that before simplification, a better understanding of the intermediate mechanisms must be developed. To do so, the extensive uncertainties in the underlying data should be addressed by a comprehensive analysis of the data already present in literature and, leading on from this, identification of key experiments to address any lack of data. This would provide a more robust framework in which models can be developed, tested, and validated.

REFERENCES

1. Hoeijmakers JHJ. Genome maintenance mechanisms for preventing cancer. Vol. 411, Nature. 2001. p. 366–74.

J_ID: RARE   Date: 17-October-23   Page: 12   Total Pages: 15

Page proofs and all forms must be returned with 72 hours of receipt.

0   WARMENHOVEN ET AL.

2. Ciccia A, Elledge SJ. The DNA Damage Response: Making It Safe to Play with Knives. Vol. 40, Molecular Cell. 2010. p. 179–204.

3. Anglada T, Terradas M, Hernández L, Genescà A, Martín M. Analysis of Residual DSBs in Ataxia-Telangiectasia Lymphoblast Cells Initiating Apoptosis. Biomed Res Int. 2016; 2016:8279560.

4. Carrano AV. Chromosome aberrations and radiation-induced cell death. Mutat Res Mol Mech Mutagen [Internet]. 1973; 17(3):341–53. Available from: http://www.sciencedirect.com/science/article/pii/0027510773900067

5. Carrano AV. Chromosome aberrations and radiation-induced cell death. II. Predicted and observed cell survival. Mutat Res - Fundam Mol Mech Mutagen. 1973; 17(3):355–66.

6. Braselmann H, Bauchinger M, Schmid E. Cell survival and radiation induced chromosome aberrations. Radiat Environ Biophys [Internet]. 1986; 25(4):243–51. Available from: http://www.springerlink.com/index/10.1007/BF01214637

7. Joiner MC, der Kogel A. Basic clinical radiobiology. CRC Press; 2016.

8. Paganetti H. Relative biological effectiveness (RBE) values for proton beam therapy. Variations as a function of biological endpoint, dose, and linear energy transfer. Phys Med Biol. 2014; 59(22):R419.

9. Gerelchuluun A, Zhu J, Su F, Asaithamby A, Chen DJ, Tsuboi K. Homologous recombination pathway may play a major role in high-LET radiation-induced DNA double-strand break repair. J Radiat Res. 2014 Mar; 55(suppl 1):i83–4.

10. Lorat Y, Brunner CU, Schanz S, Jakob B, Taucher-Scholz G, Rübe CE. Nanoscale analysis of clustered DNA damage after high-LET irradiation by quantitative electron microscopy - The heavy burden to repair. DNA Repair (Amst) [Internet]. 2015; 28:93–106. Available from: http://dx.doi.org/10.1016/j.dnarep.2015.01.007

11. Blakely EA, Tobias CA, Yang TC, Smith KC, Lyman JT. Inactivation of human kidney cells by high-energy monoenergetic heavy-ion beams. Radiat Res. 1979 Oct; 80(1):122–60.

12. Furusawa Y, Fukutsu K, Aoki M, Itsukaichi H, Eguchi-Kasai K, Ohara H, et al. Inactivation of aerobic and hypoxic cells from three different cell lines by accelerated 3He-, 12C- and 20Ne-Ion beams. Radiat Res. 2000.

13. Tsuruoka C, Suzuki M, Kanai T, Fujitaka K. LET and ion species dependence for cell killing in normal human skin fibroblasts. Radiat Res. 2005; 163:494–500.

14. Friedrich T, Durante M, Scholz M. Particle species dependence of cell survival RBE: Evident and not negligible. Acta Oncologica. 2013; 52:589–603.

15. Friedrich T, Scholz U, Elsässer T, Durante M, Scholz M. Systematic analysis of RBE and related quantities using a database of cell survival experiments with ion beam irradiation. J Radiat Res. 2013; 54:494–514.

16. Korcyl M, Waligórski MPR. Track structure effects in a study of cell killing in normal human skin fibroblasts. Int J Radiat Biol. 2009; 85:1101–13.

17. Bryant HE, Schultz N, Thomas HD, Parker KM, Flower D, Lopez E, et al. Specific killing of BRCA2-deficient tumours with inhibitors of poly(ADP-ribose) polymerase. Nature. 2005; 434(7035):913–7.

18. Farmer H, McCabe N, Lord CJ, Tutt ANJ, Johnson DA, Richardson TB, et al. Targeting the DNA repair defect in BRCA mutant cells as a therapeutic strategy. Nature [Internet]. 2005; 434(7035):917–21. Available from: http://www.nature.com/doifinder/10.1038/nature03445

19. Gudmundsdottir K, Ashworth A. The roles of BRCA1 and BRCA2 and associated proteins in the maintenance of genomic stability. Oncogene. 2006; 25(43):5864–74.

20. Pierce AJ, Jasin M. NHEJ deficiency and disease. Mol Cell. 2001; 8(6):1160–1.

21. Stewart RD, Carlson DJ, Butkus MP, Hawkins R. A comparison of mechanism-inspired models for particle relative biological effectiveness (RBE). 2018; 45(11):925–52.

22. Friedland W, Schmitt E, Kundrát P, Dingfelder M, Baiocco G, Barbieri S, et al. Comprehensive track-structure based evaluation of DNA damage by light ions from radiotherapy-relevant energies down to stopping. Sci Rep. 2017 Mar; 7(April):45161.

23. McMahon SJ. The linear quadratic model: Usage, interpretation and challenges. Phys Med Biol. 2019; 64(1).

24. Belov OV, Krasavin EA, Lyashko MS, Batmunkh M, Sweilam NH. A quantitative model of the major pathways for radiation-induced DNA double-strand break repair. J Theor Biol [Internet]. 2014; 366: 115–30. Available from: http://dx.doi.org/10.1016/j.jtbi.2014.09.024

25. Dolan D, Nelson G, Zupanic A, Smith G, Shanley D. Systems Modelling of NHEJ Reveals the Importance of Redox Regulation of Ku70/80 in the Dynamics of DNA Damage Foci. PLoS One. 2013; 8(2).

26. Dolan DWP, Zupanic A, Nelson G, Hall P, Miwa S, Kirkwood TBL, et al. Integrated Stochastic Model of DNA Damage Repair by Non-homologous End Joining and p53/p21- Mediated Early Senescence Signalling. PLoS Comput Biol. 2015; 11(5):1–19.

27. Butts JJ, Katz R. Theory of RBE for Heavy Ion Bombardment of Dry Enzymes and Viruses. Radiat Res [Internet]. 1967; 30(4):855. Available from: http://www.jstor.org/stable/3572151?origin=crossref

28. Katz R, Ackerson B, Homayoonfar M, Sharma SC. Inactivation of Cells by Heavy Ion Bombardment. Radiat Res [Internet]. 1971; 47(2):402–25. Available from: http://www.rrjournal.org/doi/abs/10.2307/3573247

29. Katz R, Sharma SC. Response of cells to fast neutrons, stopped pions, and heavy ion beams. Nucl Inst Meth. 1973; 111(1):93–116.

30. Katz R, Sharma SC. Heavy Particles in Therapy: An Application of Track Theory Heavy Particles in Therapy: An Application of Track Theory. 1974.

31. Sachs K, Levy D, Chen AM, Ingerman EA, Simpson PJ, Cornforth MN, et al. Random breakage and reunion chromosome aberration formation model; an interaction distance version based on chromatin geometry. Int J Radiat Biol. 2000; 76(12):1579–88.

32. Takahashi A, Yamakawa N, Kirita T, Omori K, Ishioka N, Furusawa Y, et al. DNA Damage Recognition Proteins Localize along Heavy Ion Induced Tracks in the Cell Nucleus. J Radiat Res [Internet]. 2008; 49(6):645–52. Available from: https://academic.oup.com/jrr/article-lookup/doi/10.1269/jrr.08007

33. Ballarini F, Ottolenghi A. Models of chromosome aberration induction: an example based on radiation track structure. Cytogenet Genome Res. 2004; 104(1–4):149–56.

34. McMahon SJ, Schuemann J, Paganetti H, Prise KM. Mechanistic Modelling of DNA Repair and Cellular Survival Following Radiation-Induced DNA Damage. Sci Rep. 2016; 6.

35. McMahon SJ, McNamara AL, Schuemann J, Paganetti H, Prise KM. A general mechanistic model enables predictions of the biological effectiveness of different qualities of radiation. Sci Rep. 2017; 7(1):10790.

36. McMahon SJ, Prise KM. A Mechanistic DNA Repair and Survival Model (Medras): Applications to Intrinsic Radiosensitivity, Relative Biological Effectiveness and Dose-Rate. Front Oncol. 2021 Jun; 11(June):1–18.

37. Carante MP, Aricò G, Ferrari A, Kozlowska W, Mairani A, Ballarini F. First benchmarking of the BIANCA model for cell survival prediction in a clinical hadron therapy scenario. Phys Med Biol. 2019 Nov; 64(21):215008.

38. Scholz M, Kraft G. Calculation of Heavy Ion Inactivation Probabilities Based on Track Structure, X Ray Sensitivity and Target Size [Internet]. Vol. 52, Radiation Protection Dosimetry. 1994. p. 29–33. Available from: http://rpd.oxfordjournals.org/content/52/1-4/29.abstract

39. Elsässer T, Weyrather WK, Friedrich T, Durante M, Iancu G, Krämer M, et al. Quantification of the relative biological effectiveness for ion beam radiotherapy: Direct experimental comparison of proton and carbon ion beams and a novel approach for treatment planning. Int J Radiat Oncol Biol Phys. 2010; 78(4):1177–83.

40. Hawkins RB. A microdosimetric-kinetic model of cell death from exposure to ionizing radiation of any LET, with experimental and clinical applications. Int J Radiat Biol. 1996 Jun; 69(6):739–55.

41. Karger CP, Peschke P. RBE and related modeling in carbon-ion therapy. Phys Med Biol. 2017 Dec; 63(1):01TR02.

42. Karamitros M, Luan S, Bernal MA, Allison J, Baldacchino G, Davidkova M, et al. Diffusion-controlled reactions modeling in Geant4-DNA. J Comput Phys. 2014; 274:841–82.

43. Delage E, Pham QT, Karamitros M, Payno H, Stepan V, Incerti S, et al. PDB4DNA: Implementation of DNA geometry from the Protein Data Bank (PDB) description for Geant4-DNA Monte-Carlo simulations. Comput Phys Commun [Internet]. 2015; 192:282–8. Available from: http://dx.doi.org/10.1016/j.cpc.2015.02.026

44. Bernal MA, Bordage MC, Brown JMC, Davídková M, Delage E, Bitar Z El, et al. Track structure modeling in liquid water: A review of the Geant4-DNA very low energy extension of the Geant4 Monte Carlo simulation toolkit. Phys Medica [Internet]. 2015; 31(8):861–74. Available from: http://www.sciencedirect.com/science/article/pii/S1120179715010042

45. Henthorn NT, Warmenhoven JW, Sotiropoulos M, Mackay RI, Kirkby KJ, Merchant MJ. Nanodosimetric Simulation of Direct Ion-Induced DNA Damage Using Different Chromatin Geometry Models. Radiat Res. 2017; 188(6):690–703.

46. Zhu H, McNamara AL, McMahon SJ, Ramos-Mendez J, Henthorn NT, Faddegon B, et al. Cellular Response to Proton Irradiation: A Simulation Study with TOPAS-nBio. Radiat Res. 2020; 194(1):9–21.

47. McNamara AL, Geng C, Turner R, Ramos-Méndez J, Perl J, Held K, et al. Validation of the radiobiology toolkit TOPAS-nBio in simple DNA geometries. Phys Medica. 2016; 33:207–15.

48. Friedland W, Paretzke HG, Ballarini F, Ottolenghi A, Kreth G, Cremer C. First steps towards systems radiation biology studies concerned with DNA and chromosome structure within living cells. Radiat Environ Biophys. 2008; 47(1):49–61.

49. Friedland W, Jacob P, Kundrat P. Mechanistic simulation of radiation damage to DNA and its repair: on the track towards systems radiation biology modelling. Radiat Prot Dosimetry. 2010; ncq383.

50. Friedland W, Jacob P, Kundrát P. Stochastic simulation of DNA double-strand break repair by non-homologous end joining based on track structure calculations. Radiat Res. 2010; 173(5):677–88.

51. Henthorn NT, Warmenhoven JW, Sotiropoulos M, Mackay RI, Kirkby NF, Kirkby KJ, et al. In Silico Non-Homologous End Joining Following Ion Induced DNA Double Strand Breaks Predicts That Repair Fidelity Depends on Break Density. Sci Rep [Internet]. 2018; 8(1):2654. Available from: http://www.nature.com/articles/s41598-018-21111-8

52. Warmenhoven JW, Henthorn NT, Ingram SP, Chadwick AL, Sotiropoulos M, Korabel N, et al. Insights into the non-homologous end joining pathway and double strand break end mobility provided by mechanistic in silico modelling. DNA Repair (Amst). 2020; 85(October 2019):102743.

53. Friedland W, Kundrát P. Track structure based modelling of chromosome aberrations after photon and alpha-particle irradiation. Mutat Res - Genet Toxicol Environ Mutagen [Internet]. 2013; 756(1–2): 213–23. Available from: http://dx.doi.org/10.1016/j.mrgentox.2013.06.013

54. Ingram SP, Henthorn NT, Warmenhoven JW, Kirkby NF, Mackay RI, Kirkby KJ, et al. Hi-C implementation of genome structure for in silico models of radiation-induced DNA damage. Ay F, editor. PLOS Comput Biol. 2020 Dec; 16(12):e1008476.

55. McNamara AL, Ramos-Mendez J, Perl J, Held K, Dominguez N, Moreno EB, et al. Geometrical structures for radiation biology research as implemented in the TOPAS-nBio toolkit. Phys Med Biol. 2018.

56. Schuemann J, McNamara AL, Warmenhoven JW, Henthorn NT, Kirkby KJ, Merchant MJ, et al. A New Standard DNA Damage (SDD) Data Format. Radiat Res. 2019 Jan; 191(1):76.

57. Incerti S, Ivanchenko A, Karamitros M, Mantero A, Moretto P, Tran HN, et al. Comparison of GEANT4 very low energy cross section models with experimental data in water. Med Phys. 2010; 37(9):4692–708.

58. Agostinelli S, Allison J, Amako K, Apostolakis J, Araujo H, Arce P, et al. GEANT4 - A simulation toolkit. Nucl Instruments Methods Phys Res Sect A Accel Spectrometers, Detect Assoc Equip. 2003; 506(3):250–303.

59. Rao SSP, Huntley MH, Durand NC, Stamenova EK, Bochkov ID, Robinson JT, et al. A 3D Map of the Human Genome at Kilobase Resolution Reveals Principles of Chromatin Looping. Cell. 2014 Dec; 159(7):1665–80.

60. Souici M, Khalil TT, Muller D, Raffy Q, Barillon R, Belafrites A, et al. Single- and double-strand breaks of dry DNA exposed to protons at bragg-peak energies. J Phys Chem B. 2017; 121(3):497–507.

61. Urushibara A, Shikazono N, O'Neill P, Fujii K, Wada S, Yokoya A. LET dependence of the yield of single-, double-strand breaks and base lesions in fully hydrated plasmid DNA films by4He2+ion irradiation. Int J Radiat Biol. 2008; 84(1):23–33.

62. Ushigome T, Shikazono N, Fujii K, Watanabe R, Suzuki M, Tsuruoka C, et al. Yield of Single- and Double-Strand Breaks and Nucleobase Lesions in Fully Hydrated Plasmid DNA Films Irradiated with High-LET Charged Particles. Radiat Res [Internet]. 2012; 177(5):614–27. Available from: http://www.bioone.org/doi/10.1667/RR2701.1

63. Vyšín L, Pachnerová Brabcová K, Štěpán V, Moretto-Capelle P, Bugler B, Legube G, et al. Proton-induced direct and indirect damage of plasmid DNA. Radiat Environ Biophys. 2015; 54(3):343–52.

64. Friedland W, Bernhardt P, Jacob P, Paretzke HG, Dingfelder M. Simulation of DNA damage after proton and low LET irradiation. Radiat Prot Dosimetry. 2002; 99:99–102.

65. Francis Z, Villagrasa C, Clairand I. Simulation of DNA damage clustering after proton irradiation using an adapted DBSCAN algorithm. Comput Methods Programs Biomed [Internet]. 2011; 101(3):265–70. Available from: http://dx.doi.org/10.1016/j.cmpb.2010.12.012

66. Henthorn NT, Warmenhoven JW, Sotiropoulos M, Aitkenhead AH, Smith EAK, Ingram SP, et al. Clinically relevant nanodosimetric simulation of DNA damage complexity from photons and protons. RSC Adv. 2019; 9(12):6845–58.

67. Schuemann J, McNamara AL, Ramos-Méndez J, Perl J, Held KD, Paganetti H, et al. TOPAS-nBio: An Extension to the TOPAS Simulation Toolkit for Cellular and Sub-cellular Radiobiology. Radiat Res. 2018 Jan; 191(2):125–38.

68. Lieberman-Aiden E, van Berkum NL, Williams L, Imakaev M, Ragoczy T, Telling A, et al. Comprehensive mapping of long-range interactions reveals folding principles of the human genome. Science. 2009 Oct; 326(5950):289–93.

69. Lampe N, Karamitros M, Breton V, Brown JMC, Sakata D, Sarramia D, et al. Mechanistic DNA damage simulations in Geant4-DNA Part 2: Electron and proton damage in a bacterial cell. Phys Medica. 2018; (October 2017):0–1.

70. Dos Santos M, Villagrasa C, Clairand I, Incerti S. Influence of the chromatin density on the number of direct clustered damages calculated for proton and alpha irradiations using a Monte Carlo code. Prog Nucl Sci Technol. 2014; 4:449–53.

71. Bordage MC, Bordes J, Edel S, Terrissol M, Franceries X, Bardiès M, et al. Implementation of new physics models for low energy electrons in liquid water in Geant4-DNA. Phys Medica. 2016 Dec; 32(12):1833–40.

72. Ramos-Méndez J, Perl J, Schuemann J, McNamara A, Paganetti H, Faddegon B. Monte Carlo simulation of chemistry following radiolysis with TOPAS-nBio. Phys Med Biol. 2018; 63(10).

73. Girst S, Hable V, Drexler GA, Greubel C, Siebenwirth C, Haum M, et al. Subdiffusion supports joining of correct ends during repair of DNA double-strand breaks. Sci Rep. 2013; 3.

J_ID: RARE Date: 17-October-23   Page: 14   Total Pages: 15

Page proofs and all forms must be returned with 72 hours of receipt.

74. Mine-Hattab J, Recamier V, Izeddin I, Rothstein R, Darzacq X. Fast imaging of DNA motion reveals distinct sub-diffusion regimes at the site of DNA damage. bioRxiv. 2016; 42051.

75. Lee K-J, Saha J, Sun J, Fattah KR, Wang S-C, Jakob B, et al. Phosphorylation of Ku dictates DNA double-strand break (DSB) repair pathway choice in S phase. Nucleic Acids Res. 2015; gkv1499.

76. Uematsu N, Weterings E, Yano K, Morotomi-Yano K, Jakob B, Taucher-Scholz G, et al. Autophosphorylation of DNA-PKCS regulates its dynamics at DNA double-strand breaks. J Cell Biol. 2007; 177(2):219–29.

77. Andrin C, McDonald D, Attwood KM, Rodrigue A, Ghosh S, Mirzayans R, et al. A requirement for polymerized actin in DNA double-strand break repair. Nucl (United States). 2012; 3(4):14.

78. Hartlerode AJ, Morgan MJ, Wu Y, Buis J, Ferguson DO. Recruitment and activation of the ATM kinase in the absence of DNA-damage sensors. Nat Struct Mol Biol. 2015; 22(9):736–43.

79. Li AYJ, Boo LM, Wang SY, Lin HH, Wang CCC, Yen Y, et al. Suppression of nonhomologous end joining repair by overexpression of HMGA2. Cancer Res. 2009; 69(14):5699–706.

80. Graham TGW, Walter JC, Loparo JJ. Two-Stage Synapsis of DNA Ends during Non-homologous End Joining. Mol Cell. 2016; 61(6):850–8.

81. Davis AJ, So S, Chen DJ. Dynamics of the PI3K-like protein kinase members ATM and DNA-PKcs at DNA double strand breaks. Cell Cycle. 2010; 9(13):2529–36.

82. Weterings E, Verkaik NS, Keijzers G, Florea BI, Wang S-Y, Ortega LG, et al. The Ku80 carboxy terminus stimulates joining and artemis-mediated processing of DNA ends. Mol Cell Biol [Internet]. 2009; 29(5):1134–42. Available from: http://www.scopus.com/inward/record.url?eid=2-s2.0-61749092799&partnerID=tZOtx3y1

83. Hammel M, Yu Y, Mahaney BL, Cai B, Ye R, Phipps BM, et al. Ku and DNA-dependent protein kinase dynamic conformations and assembly regulate DNA binding and the initial non-homologous end joining complex. J Biol Chem. 2010; 285(2):1414–23.

84. Chaudhary P, Marshall TI, Currell FJ, Kacperek A, Schettino G, Prise KM. Variations in the processing of DNA double-strand breaks along 60-MeV therapeutic proton beams. Int J Radiat Oncol Biol Phys. 2016; 95(1):86–94.

85. Smith EAK, Henthorn NT, Warmenhoven JW, Ingram SP, Aitkenhead AH, Richardson JC, et al. In Silico Models of DNA Damage and Repair in Proton Treatment Planning: A Proof of Concept. Sci Rep. 2019; 9(1):1–10.

86. Meylan S, Incerti S, Karamitros M, Tang N, Bueno M, Clairand I, et al. Simulation of early DNA damage after the irradiation of a fibroblast cell nucleus using Geant4-DNA. Sci Rep. 2017; 7(1):1–15.

87. Friedland W, Jacob P, Bernhardt P, Paretzke HG, Dingfelder M. Simulation of DNA Damage after Proton Irradiation. Radiat Res [Internet]. 2003; 159(3):401–10. Available from: http://www.bioone.org/doi/abs/10.1667/0033-7587(2003)159[0401:SODDAP]2.0.CO; 2

88. Roots R, Okada S. Estimation of Life Times and Diffusion Distances of Radicals Involved in X-Ray-Induced DNA Strand Breaks or Killing of Mammalian Cells. Radiat Res. 1975 Nov; 64(2):306.

89. Graham TGW, Walter JC, Loparo JJ. Two-Stage Synapsis of {DNA} Ends during Non-homologous End Joining. Mol Cell [Internet]. 2016; 61(6):850–8. Available from: http://www.sciencedirect.com/science/article/pii/S1097276516000940

90. Soutoglou E, Dorn JF, Sengupta K, Jasin M, Nussenzweig A, Ried T, et al. Positional stability of single double-strand breaks in mammalian cells. Nat Cell Biol. 2007; 9(6):675–82.

91. McNamara A, Geng C, Turner R, Mendez JR, Perl J, Held K, et al. Validation of the radiobiology toolkit TOPAS-nBio in simple DNA geometries. Phys Medica. 2017; 33:207–15.

92. Elsässer T, Scholz M. Cluster effects within the local effect model. Radiat Res. 2007.

93. Nikjoo H, O'Neill P, Terrissol M, Goodhead DT. Quantitative modelling of DNA damage using Monte Carlo track structure method. Radiat Environ Biophys. 1999.

94. Sakata D, Lampe N, Karamitros M, Kyriakou I, Belov O, Bernal MA, et al. Evaluation of early radiation DNA damage in a fractal cell nucleus model using Geant4-DNA. Phys Medica. 2019.

95. McMahon SJ, Prise KM. A Mechanistic DNA Repair and Survival Model (Medras): Applications to Intrinsic Radiosensitivity, Relative Biological Effectiveness and Dose-Rate. Front Oncol. 2021.

AQ: 1

AUTHOR QUERIES

AUTHOR PLEASE ANSWER ALL QUERIES   1

AQau—Please make certain that all authors' names are spelled correctly, and confirm the given-names and surnames are identified properly by the colors (this is important for how the names are indexed).

■= Given-Name, ■= Surname

AQ1—Please check references numbers [86 and 95] are not cited in article body.